LETTER

doi:10.1038/nature25182

Opening of the human epithelial calcium channel TRPV6

Luke L. McGoldrick[1,2]*, Appu K. Singh[1]*, Kei Saotome[1], Maria V. Yelshanskaya[1], Edward C. Twomey[1,2], Robert A. Grassucci[1] & Alexander I. Sobolevsky[1]

Calcium-selective transient receptor potential vanilloid subfamily member 6 (TRPV6) channels play a critical role in calcium uptake in epithelial tissues[1–4]. Altered TRPV6 expression is associated with a variety of human diseases[5], including cancers[6]. TRPV6 channels are constitutively active[1,7,8] and their open probability depends on the lipidic composition of the membrane in which they reside; it increases substantially in the presence of phosphatidylinositol 4,5-bisphosphate[7,9]. Crystal structures of detergent-solubilized rat TRPV6 in the closed state have previously been solved[10,11]. Corroborating electrophysiological results[3], these structures demonstrated that the Ca^{2+} selectivity of TRPV6 arises from a ring of aspartate side chains in the selectivity filter that binds Ca^{2+} tightly. However, how TRPV6 channels open and close their pores for ion permeation has remained unclear. Here we present cryo-electron microscopy structures of human TRPV6 in the open and closed states. The channel selectivity filter adopts similar conformations in both states, consistent with its explicit role in ion permeation. The iris-like channel opening is accompanied by an α-to-π-helical transition in the pore-lining transmembrane helix S6 at an alanine hinge just below the selectivity filter. As a result of this transition, the S6 helices bend and rotate, exposing different residues to the ion channel pore in the open and closed states. This gating mechanism, which defines the constitutive activity of TRPV6, is, to our knowledge, unique among tetrameric ion channels and provides structural insights for understanding their diverse roles in physiology and disease.

We expressed the full-length human TRPV6 (hTRPV6) channel in HEK 293 cells, where it exhibited typical Ca^{2+} permeability[12] (Fig. 1a, b) and current–voltage relationships[13–17] (Extended Data Fig. 1a). To structurally characterize hTRPV6, we purified it separately in nanodiscs and amphipols (see Methods) and solved the corresponding structures using cryo-electron microscopy (cryo-EM; Extended Data Figs 2, 3 and Extended Data Table 1) to 3.6 Å and 4.0 Å, respectively. Although the reconstructions in nanodiscs and amphipols were nearly identical, the structure solved in nanodiscs had better overall resolution and will be our primary descriptor of hTRPV6. Two-dimensional class averages showed diverse orientations and easily discernible secondary structure features (Fig. 1c). The resulting 3D reconstruction (Fig. 1d, e) showed higher resolution features for the core of the molecule than for its periphery (Extended Data Fig. 2c) and was of sufficient quality (Extended Data Fig. 4) to build each subunit (residues 28–638) of the hTRPV6 homotetramer *de novo*.

The structure of hTRPV6 (Fig. 2a, b) has the same overall architecture as that of rat TRPV6 (rTRPV6)[10]. Whereas no discernible lipid densities were observed in the crystal structures of rTRPV6[10,11], the hTRPV6 cryo-EM reconstruction reveals 16 (4 per subunit) well-resolved non-protein densities that are intercalated in subunit interfaces and are likely to represent lipids (Fig. 2c). Similarly positioned densities in the structure of TRPV1[18] were modelled with phosphatidylinositol, phosphatidylcholine and phosphatidylethanolamine lipids. Of the four putative lipid densities in hTRPV6, the fourth density has a clear

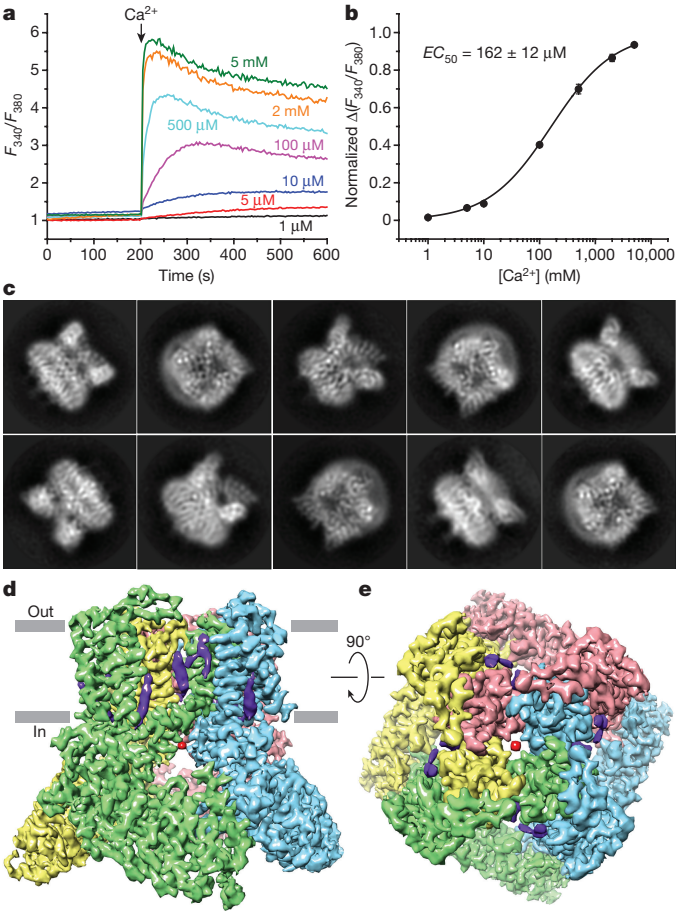

Figure 1 | Function and cryo-EM of hTRPV6. a, **b**, Functional characterization of hTRPV6 using ratiometric fluorescence measurements. **a**, Fluorescence curves recorded from HEK 293 cells expressing hTRPV6 in response to the application of Ca^{2+} (arrow) at different concentrations. These experiments were repeated independently three times with similar results. **b**, Ca^{2+} dose–response curve for the maximal value of fluorescence fitted with the logistic equation. The calculated half maximal effective concentration (EC_{50}) is shown as mean ± s.e.m. ($n = 3$). **c**, Two-dimensional class averages of hTRPV6 particles, showing diverse orientations. **d**, **e**, hTRPV6 3.6 Å cryo-EM reconstruction, with density shown at 0.035 threshold level (UCSF Chimera) representing hTRPV6 subunits coloured green, cyan, pink and yellow, lipid in purple and ions in red.

[1]Department of Biochemistry and Molecular Biophysics, Columbia University, 650 West 168th Street, New York, New York 10032, USA. [2]Integrated Program in Cellular, Molecular, and Biomedical Studies, Columbia University, 650 West 168th Street, New York, New York 10032, USA.
*These authors contributed equally to this work.

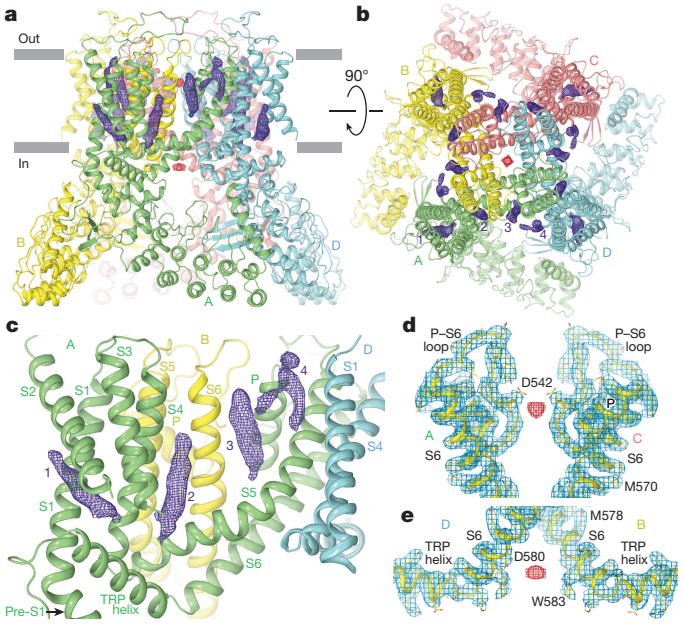

Figure 2 | Structure of hTRPV6. a, **b**, Side (**a**) and top (**b**) views of hTRPV6 tetramer, with each subunit (A–D) shown in a different colour. Putative lipid densities at 3.5σ and ion densities at 4σ are illustrated by purple and red mesh, respectively. **c**, Expanded view of the four (1–4) putative lipid densities per hTRPV6 subunit. **d**, **e**, Expanded views of the putative ion densities at 4σ at the selectivity filter (**d**) and S6 helices bundle crossing (**e**).

head-and-two-tails appearance. Fitting different lipid molecules into density 4 (Extended Data Fig. 5a–c) suggests that the chemical environment around the lipid head group, including the negatively charged aspartate D525 and polar Y349, Y509, Q513 and Y524 residues, supports binding of phosphatidylethanolamine or phosphatidylcholine rather than phosphatidylinositol 4,5-bisphosphate (PtdIns(4,5)P_2). Densities 1–3 have sausage-like appearances and might represent a wider variety of lipid-like molecules, including cholesterol or cholesterol hemisuccinate (CHS) (Extended Data Fig. 5d, e). In physiological conditions, some of these sites can bind PtdIns(4,5)P_2[7,9]. For example, the positively charged R470 and K484 and polar T479, Q483 and Q596 residues around density 2 create a permissive chemical environment for the negatively charged head group of PtdIns(4,5)P_2. However, the poor fit of PtdIns(4,5)P_2 into density 2 (Extended Data Fig. 5f) suggests that in our cryo-EM structure, density 2 represents a different molecule.

In the crystal structure of rTRPV6 in the closed state, the M577 side chains form a hydrophobic 'seal' on the cytoplasmic side of the S6 helices[10,11]. By contrast, interatomic distances within the pore of the new structure confirmed that the hTRPV6 channel pore is open (Fig. 3). The pore surface is lined by the side chains of D542, T539, N572, I575, D580 and W583, as well as the backbone-carbonyl oxygens of I540, I541 and G579. The narrowest part of the upper pore, the selectivity filter, is formed by the D542 side chains, one from each subunit, which project towards the centre of the pore (Fig. 3a, c, f). We propose that D542 in hTRPV6, similar to D541 in rTRPV6, plays an important role in Ca^{2+} permeation by directly coordinating dehydrated Ca^{2+} ions[11]. The narrowest part of the hTRPV6 lower pore (9.6 Å interatomic distance) is defined by the side chains of I575 at the S6 bundle crossing (Fig. 3a, c, d). This part of the pore is comparable in size to the pore of open TRPV1 (9.3 Å interatomic distance, measured between side chains of I679)[18] and is wide open for conductance of hydrated Na^+ or Ca^{2+} ions.

Along the axis of the hTRPV6 pore, there is a strong density about 3.9 Å away from the side chains of D542 (Fig. 2d) that is likely to represent a Ca^{2+} ion bound to a site homologous to the main Ca^{2+}-binding site (site 1) at D541 in the pore of rTRPV6[10,11]. An additional strong density along the hTRPV6 pore is observed at the bundle crossing of the S6 helices, about 8.0 Å away from D580 and about 6.6 Å away from W583, suggesting that these residues may play an important role in ion permeation (Fig. 2e). Indeed, W583 is conserved in TRPV6 and TRPV5 channels and is involved in the regulation of calcium uptake, as shown by mutation W583A in TRPV5, which induces cell death due to increased calcium influx[19]. The density at the S6 helices bundle crossing, which was not observed in the pore of the closed-state rTRPV6[10,11], is likely to represent another permeant ion bound in the open pore of hTRPV6.

To determine the structure of hTRPV6 in the closed state, we decided to shift the open–closed state gating equilibrium towards the closed state by interfering with channel activation. Because the open probability of TRPV6 is strongly dependent on membrane lipids[7,9], altering lipid binding by mutagenesis might result in channel closure. TRPV1, for example, is activated through an intramembrane vanilloid-binding site (Fig. 4a), which accommodates agonists, such as resiniferatoxin (RTX) and capsaicin, and antagonists, such as capsazepine (CPZ)[18]. In the absence of ligands, this site is occupied by the lipid phosphatidylinositol, which favours the closed pore conformation[18]. The TRPV1 vanilloid-binding site coincides with hTRPV6 lipid density 2, which may represent the binding site for natural lipid agonists (Fig. 4b).

To test whether this site is critical for channel activation, we mutated R470 to glutamate (R470E). An analogous mutation has previously been shown to eliminate capsaicin-evoked currents in TRPV1[20]. The mutant hTRPV6(R470E) channels were functional (Extended Data Fig. 1b) but their calcium uptake was about ten times slower than that of wild-type channels (Extended Data Fig. 1e, f), consistent with their less frequent openings. In addition, 2-APB, a TRPV6 inhibitor that acts through the membrane, showed increased affinity to and decreased maximum inhibition of hTRPV6(R470E) compared to wild-type channels (Extended Data Fig. 1i–k), consistent with the R470E mutation altering regulation of TRPV6 by lipids.

We solved the hTRPV6(R470E) structure in amphipols by cryo-EM to 4.2 Å resolution (Extended Data Fig. 6). Consistent with the idea that the site 2 density represents an activating lipid, this density was smaller in hTRPV6(R470E) (Fig. 4c) than in hTRPV6 (Fig. 4b). Confirming that the physical occupancy of site 2 differed, the side chain of Q483 in hTRPV6(R470E) has an altered conformation that would cause clashing with the lipid density in wild-type hTRPV6 (Fig. 4b, c). Supporting the role of Q483 in lipid recognition, an hTRPV6(Q483A) mutant, while being functional (Extended Data Fig. 1c), showed an approximately five times slower calcium uptake than wild-type channels (Extended Data Fig. 1e, g). Notably, the ion channel in hTRPV6(R470E) appears to be closed (Fig. 3b, c, e). Indeed, the size of the pore at the S6 bundle crossing becomes comparable to the narrowest point of the selectivity filter. While the latter is formed by the side chains of D542, which directly coordinate calcium ions for selective permeation, the S6 bundle crossing is formed by the side chains of L574 and M578, which create a hydrophobic seal impermeable to ions and water, and therefore represent the channel gate.

The closed-state structure of hTRPV6(R470E) is nearly identical to the closed-state crystal structure of rat TRPV6 (rTRPV6)[10] and their superposition yields a root mean square deviation (r.m.s.d.) of 0.917 Å. To verify that the rTRPV6 crystal structure represents the physiologically relevant conformation, we solved the structure of rTRPV6 by cryo-EM to 3.9 Å using a lipid nanodisc preparation similar to that used for hTRPV6 (Extended Data Fig. 7). Strikingly, the cryo-EM structure of rTRPV6 is nearly identical (r.m.s.d. = 0.781 Å) to the crystal structure of rTRPV6 (Extended Data Fig. 8a–c). As the hTRPV6(R470E) structure is nearly identical to both the rTRPV6 cryo-EM structure (Extended Data Fig. 8d, e, r.m.s.d. = 0.932 Å) and the rTRPV6 crystal structure, we contend that it represents the true closed state of hTRPV6. Consistently, a much weaker density at site 2 in the cryo-EM structure of rTRPV6 (Fig. 4d) suggests either lower occupancy or greater

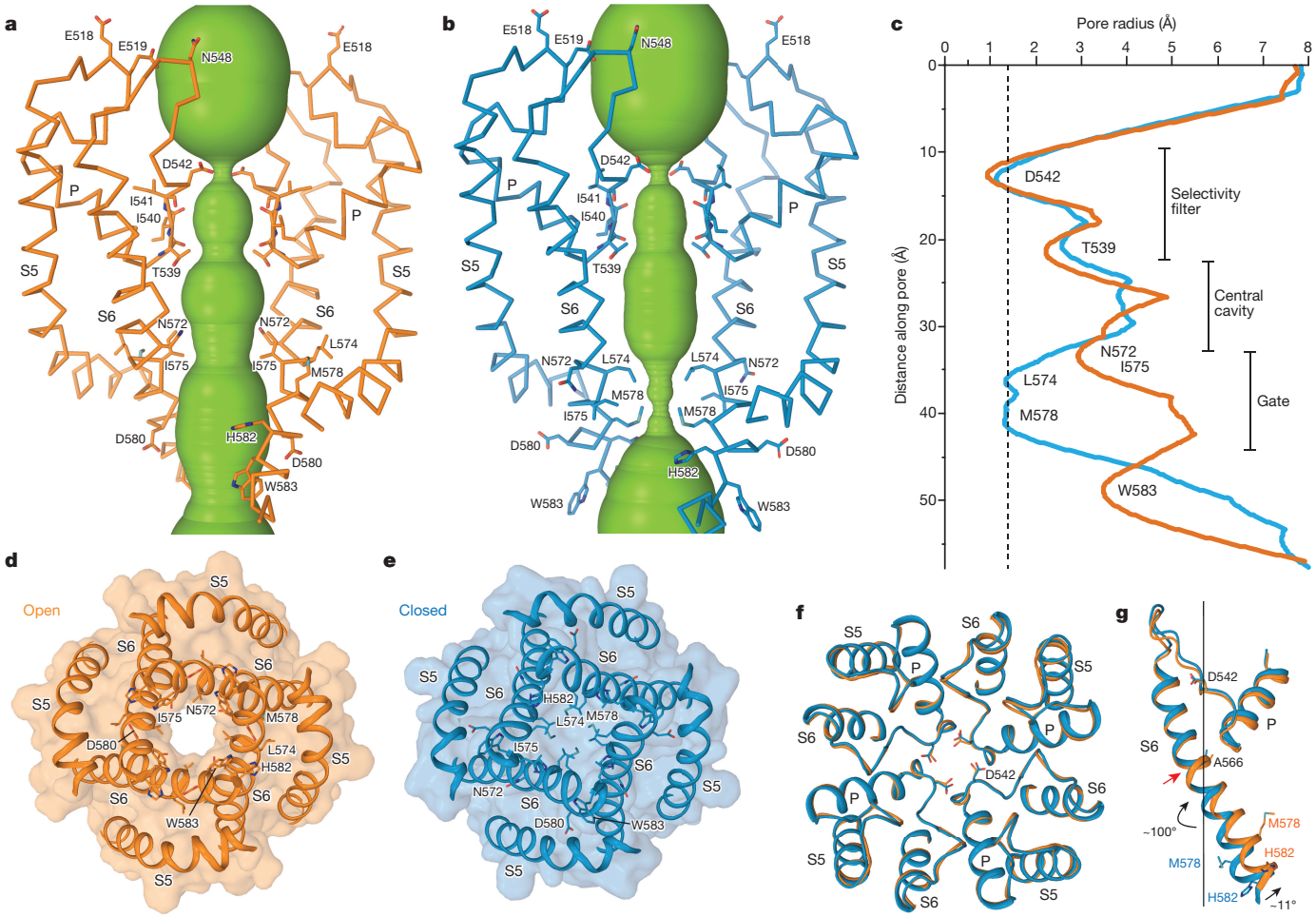

Figure 3 | Open and closed ion channel pore. a, **b**, Ion conduction pathway (green) in open hTRPV6 (**a**) and closed hTRPV6(R470E) (**b**), with residues lining the selectivity filter and around the gate shown as sticks. Only two of four subunits are shown, with the front and back subunits removed for clarity. **c**, Pore radius calculated using HOLE[29] for hTRPV6 (orange) and hTRPV6(R470E) (blue). Dashed line corresponds to 1.4 Å (radius of a water molecule). **d**, **e**, Intracellular view of the S6 bundle crossing in hTRPV6 (**d**) and hTRPV6(R470E) (**e**). **f**, Superposition of the selectivity filter regions in hTRPV6 (orange) and hTRPV6(R470E) (blue), viewed extracellularly. **g**, Superposition of the P loop and S6 in hTRPV6 (orange) and hTRPV6(R470E) (blue), viewed parallel to the membrane. The straight line shows the pore axis, red arrow indicates the position of the gating hinge alanine A566 and black arrows illustrate ~100° rotation and ~11° bending away from the pore axis of the C-terminal part of S6.

mobility of the putative bound lipid. Because rTRPV6 and hTRPV6 were purified in similar conditions, have 89% overall sequence identity, and have identical amino acid compositions of their site 2 lipid-binding pockets, it remains unclear why one channel was closed and the other open. For example, some lipids within the membranes of the protein-expressing HEK 293 cells may be important for opening of hTRPV6 but not rTRPV6. Different conformations of rTRPV6 and hTRPV6 might also reflect the ease with which these constitutively active channels rapidly transition between gating states, and that very subtle changes can push this equilibrium towards one state or the other.

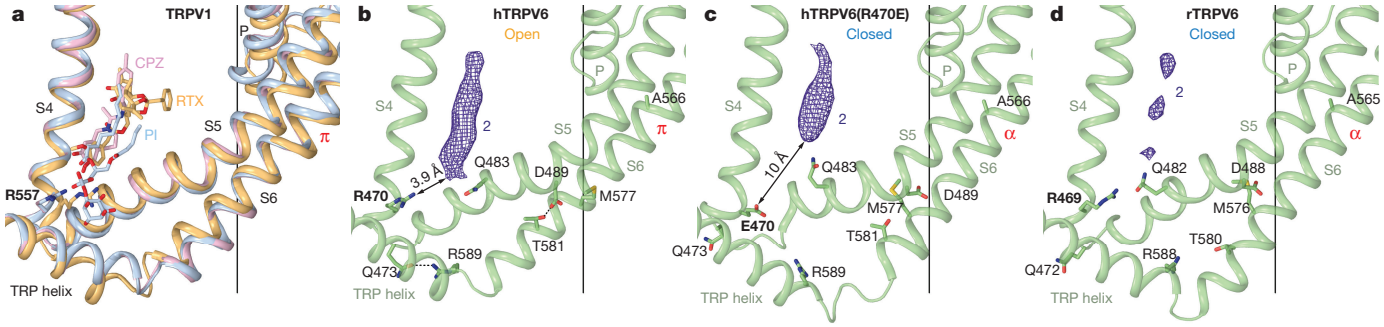

Figure 4 | Activation-related lipid binding pocket. a, Superposition of the agonist binding site in TRPV1 structures in the phosphatidylinositol (PI)-bound closed state (blue, PDB ID: 5IRZ), antagonist CPZ-bound closed state (pink, PDB ID: 5IS0) and agonist RTX-bound open state (orange, PDB ID: 5IRX). **b**–**d**, Putative activating lipid binding site in open hTRPV6 (**b**), closed hTRPV6(R470E) (**c**) and closed rTRPV6 (**d**), with densities filtered to the same resolution (4.24 Å) and shown at 5.3σ as purple mesh. Residues involved in gating are shown as sticks. Dashed lines in **b** indicate bonds between the residues.

Such subtle changes, for instance, can originate from different interactions of the membrane-mimicking environment (amphipols or nanodiscs) with helices S1–S3. These helices contain the largest number of membrane lipid-facing residues (69%), of which only 80% are identical between rTRPV6 and hTRPV6.

To understand the structural changes that occur during TRPV6 opening, we compared our hTRPV6(R470E) and hTRPV6 structures. The principal changes occur in the pore-lining helix S6 and originate at A566, which is highly conserved in TRPV5 and TRPV6 (Extended Data Fig. 9k) and located right below the selectivity filter (Fig. 3g). Confirming its important role in gating, substitution of A566 with threonine, the homologous residue conserved in TRPV1–4, greatly reduced the TRPV6 current amplitude (Extended Data Fig. 1d) and slowed calcium uptake by approximately 30 times (Extended Data Fig. 1e, h). Upon opening, S6, which has an α-helical conformation in the closed state, undergoes a local transition to a π-helix. Notably, such a transition has been hypothesized previously, based on a comparison between the TRPV1 and TRPV2 structures[21]. Concurrently, the lower part of S6, which forms the gate in the closed state, rotates by about 100° and bends away from the pore axis by about 11° (Fig. 3g). These rearrangements not only widen the pore for permeant ions but also change the set of residues that face the pore axis (for example, N572 and I575 in the open state compared to L574 and M578 in the closed state). Alanine A566, therefore, acts as a hinge to allow TRPV6 gating at the S6 bundle crossing without changing the conformation of the selectivity filter (Fig. 3f). Correspondingly, the selectivity filter appears to play a crucial role in TRPV6 channel ion permeation rather than gating. Gating-related conformational changes induced by the α-to-π-helical transition in S6 seem to involve only the intracellular portions of S5 and S6, the S4–S5 linker and the TRP helix. Indeed, superposition of the corresponding regions (residues 469–500 plus 566–608) in hTRPV6 and hTRPV6(R470E) gives an r.m.s.d. of 1.74 Å, while the rest of the molecules superpose with a much lower r.m.s.d. of 0.218 Å.

Within the regions involved in gating, pore opening in hTRPV6 is accompanied by the formation of two electrostatic bonds per subunit (Fig. 4b). A salt bridge forms between Q473 in the S4–S5 elbow and R589 in the TRP helix, and a hydrogen bond forms between D489 in the S5 helix and T581 in the S6 helix. Neither interaction is present in the closed-state structures of hTRPV6(R470E) or rTRPV6 and the formation of the hydrogen bond (D489–T581 in hTRPV6(R470E) or D488–T580 in rTRPV6) is prevented by the side chain of M577 or M576, respectively (Fig. 4c, d, Extended Data Fig. 8f, g). The importance of the D489–T581 interaction for hTRPV6 opening is supported by the previous observation that a mutation equivalent to T581A reduces the excessive constitutive activity of an hTRPV6(G516S) mutant[22]. We speculate that formation of the electrostatic bonds compensates for the energetic cost of the unfavourable α-to-π-helical transition in S6 during channel opening. This structural solution therefore maintains the relative stabilities and similar energy levels of both gating states and supports the constitutive activity of TRPV6. Accordingly, the open and closed conformations of TRPV6 remain in a readily tunable equilibrium that can be shifted towards either state by different stimuli, including lipids[7,9].

Our structures of hTRPV6 reveal a gating mechanism that is novel among tetrameric ion channels (Fig. 5, Supplementary Video 1). Although other representatives of the TRP channel family have a local α-to-π-helical transition in the middle of S6[18,23–25], they lack the alanine gating hinge (Extended Data Fig. 9). As a result, S6 maintains its secondary structure throughout the entire TRPV1 gating cycle, the same residues face the pore in the closed and open states, and pore widening is observed at both the S6 bundle crossing and the selectivity filter[18]. On the other hand, K^+ channels do have a gating hinge in their pore-forming inner helices[26,27]. However, this hinge is formed by a glycine located one residue C-terminally compared to the gating hinge alanine in TRPV6 and permits bending of the inner helices by about 30° without an α-to-π transition. The glycine hinge, like the alanine hinge in TRPV6, allows gating of K^+ channels to occur at the inner helices bundle crossing without changing the selectivity filter. However, unlike TRPV6, the glycine gating hinge in K^+ channels does not introduce a 100° rotation of the lower parts of the pore-forming helices and correspondingly does not change the residues that line the pore gate region. An alanine gating hinge is present in the pore-forming helices of ionotropic glutamate receptor (iGluR) family tetrameric ion channels[28]. However, this alanine gating hinge is located at the ion channel gate region. Correspondingly, bending the pore-forming helices at the iGluR alanine gating hinge directly alters the diameter of the pore in close proximity to the gate without an α-to-π transition. The alanine gating hinge in TRPV5 and TRPV6 channels is therefore a unique structural element that is likely to be associated with their exclusive physiological role as constitutively active calcium uptake channels.

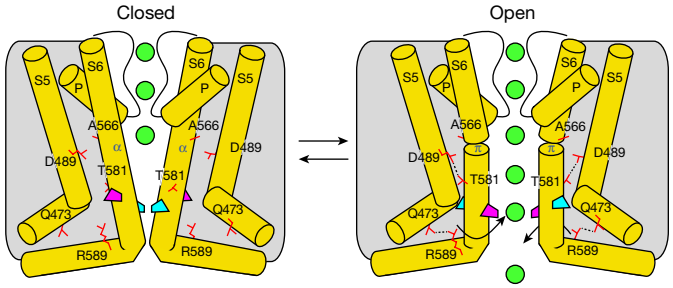

Figure 5 | TRPV6 channel gating mechanism. Cartoons represent the structural changes associated with TRPV6 channel gating. Transition from the closed to open state, stabilized by the formation of salt bridges (dashed lines), leads to permeation of ions (green spheres) and is accompanied by a local α-to-π-helical transition in S6 that maintains the selectivity filter conformation, while the lower part of S6 bends by about 11° and rotates by about 100°. These movements result in a different set of residues (cyan versus pink symbols) lining the pore in the vicinity of the channel gate.

Online Content Methods, along with any additional Extended Data display items and Source Data, are available in the online version of the paper; references unique to these sections appear only in the online paper.

Received 14 August; accepted 28 November 2017.
Published online 20 December 2017.

1. Peng, J. B. *et al.* Molecular cloning and characterization of a channel-like transporter mediating intestinal calcium absorption. *J. Biol. Chem.* **274,** 22739–22746 (1999).
2. Yue, L., Peng, J. B., Hediger, M. A. & Clapham, D. E. CaT1 manifests the pore properties of the calcium-release-activated calcium channel. *Nature* **410,** 705–709 (2001).
3. Owsianik, G., Talavera, K., Voets, T. & Nilius, B. Permeation and selectivity of TRP channels. *Annu. Rev. Physiol.* **68,** 685–717 (2006).
4. Woudenberg-Vrenken, T. E. *et al.* Functional TRPV6 channels are crucial for transepithelial Ca^{2+} absorption. *Am. J. Physiol. Gastrointest. Liver Physiol.* **303,** G879–G885 (2012).
5. Fecher-Trost, C., Weissgerber, P. & Wissenbach, U. TRPV6 channels. *Handb. Exp. Pharmacol.* **222,** 359–384 (2014).
6. Lehen'kyi, V., Raphaël, M. & Prevarskaya, N. The role of the TRPV6 channel in cancer. *J. Physiol. (Lond.)* **590,** 1369–1376 (2012).
7. Zakharian, E., Cao, C. & Rohacs, T. Intracellular ATP supports TRPV6 activity via lipid kinases and the generation of $PtdIns(4,5)P_2$. *FASEB J.* **25,** 3915–3928 (2011).
8. den Dekker, E., Hoenderop, J. G., Nilius, B. & Bindels, R. J. The epithelial calcium channels, TRPV5 & TRPV6: from identification towards regulation. *Cell Calcium* **33,** 497–507 (2003).
9. Velisetty, P. *et al.* A molecular determinant of phosphoinositide affinity in mammalian TRPV channels. *Sci. Rep.* **6,** 27652 (2016).
10. Singh, A. K., Saotome, K. & Sobolevsky, A. I. Swapping of transmembrane domains in the epithelial calcium channel TRPV6. *Sci. Rep.* **7,** 10669 (2017).
11. Saotome, K., Singh, A. K., Yelshanskaya, M. V. & Sobolevsky, A. I. Crystal structure of the epithelial calcium channel TRPV6. *Nature* **534,** 506–511 (2016).
12. Bödding, M. & Flockerzi, V. Ca^{2+} dependence of the Ca^{2+}-selective TRPV6 channel. *J. Biol. Chem.* **279,** 36546–36552 (2004).
13. Hoenderop, J. G., Nilius, B. & Bindels, R. J. Calcium absorption across epithelia. *Physiol. Rev.* **85,** 373–422 (2005).

14. Hoenderop, J. G. *et al.* Function and expression of the epithelial Ca^{2+} channel family: comparison of mammalian ECaC1 and 2. *J. Physiol. (Lond.)* **537,** 747–761 (2001).
15. Kovacs, G. *et al.* Inhibition of the human epithelial calcium channel TRPV6 by 2-aminoethoxydiphenyl borate (2-APB). *Cell Calcium* **52,** 468–480 (2012).
16. Fecher-Trost, C. *et al.* The *in vivo* TRPV6 protein starts at a non-AUG triplet, decoded as methionine, upstream of canonical initiation at AUG. *J. Biol. Chem.* **288,** 16629–16644 (2013).
17. Voets, T., Janssens, A., Prenen, J., Droogmans, G. & Nilius, B. Mg^{2+}-dependent gating and strong inward rectification of the cation channel TRPV6. *J. Gen. Physiol.* **121,** 245–260 (2003).
18. Gao, Y., Cao, E., Julius, D. & Cheng, Y. TRPV1 structures in nanodiscs reveal mechanisms of ligand and lipid action. *Nature* **534,** 347–351 (2016).
19. van der Wijst, J. *et al.* A gate hinge controls the epithelial calcium channel TRPV5. *Sci. Rep.* **7,** 45489 (2017).
20. Boukalova, S., Marsakova, L., Teisinger, J. & Vlachova, V. Conserved residues within the putative S4–S5 region serve distinct functions among thermosensitive vanilloid transient receptor potential (TRPV) channels. *J. Biol. Chem.* **285,** 41455–41462 (2010).
21. Zubcevic, L. *et al.* Cryo-electron microscopy structure of the TRPV2 ion channel. *Nat. Struct. Mol. Biol.* **23,** 180–186 (2016).
22. Hofmann, L., Wang, H., Beck, A., Wissenbach, U. & Flockerzi, V. A conserved gating element in TRPV6 channels. *Cell Calcium* **63,** 24–28 (2017).
23. Paulsen, C. E., Armache, J. P., Gao, Y., Cheng, Y. & Julius, D. Structure of the TRPA1 ion channel suggests regulatory mechanisms. *Nature* **520,** 511–517 (2015).
24. Huynh, K. W. *et al.* Structure of the full-length TRPV2 channel by cryo-EM. *Nat. Commun.* **7,** 11130 (2016).
25. Shen, P. S. *et al.* The structure of the polycystic kidney disease channel PKD2 in lipid nanodiscs. *Cell* **167,** 763–773.e11 (2016).
26. Jiang, Y. *et al.* The open pore conformation of potassium channels. *Nature* **417,** 523–526 (2002).
27. Jiang, Y. *et al.* X-ray structure of a voltage-dependent K^+ channel. *Nature* **423,** 33–41 (2003).
28. Twomey, E. C., Yelshanskaya, M. V., Grassucci, R. A., Frank, J. & Sobolevsky, A. I. Channel opening and gating mechanism in AMPA-subtype glutamate receptors. *Nature* **549,** 60–65 (2017).
29. Smart, O. S., Neduvelil, J. G., Wang, X., Wallace, B. A. & Sansom, M. S. HOLE: a program for the analysis of the pore dimensions of ion channel structural models. *J. Mol. Graph.* **14,** 354–360, 376 (1996).

Supplementary Information is available in the online version of the paper.

Acknowledgements We thank T. Rohacs for advice on electrophysiological recordings, J. Frank for comments on the manuscript, H. Kao for computational support and members of the E.C. Greene laboratory for assistance with their fluorimeter. L.L.M. and E.C.T. are supported by the NIH (T32 GM008224 and F31 NS093838, respectively). A.I.S. is supported by the NIH (R01 CA206573, R01 NS083660), and Amgen Young Investigator and Irma T. Hirschl Career Scientist awards. Data were collected at the Columbia University Medical Center cryo-EM facility and at the Simons Electron Microscopy Center and National Resource for Automated Molecular Microscopy located at the New York Structural Biology Center, supported by grants from the Simons Foundation (349247), NYSTAR, and the NIH (GM103310).

Author Contributions L.L.M., A.K.S. and A.I.S. designed the project, built models and analysed data. L.L.M. and A.K.S. carried out Fura-2 experiments, cryo-EM data collection and processing. L.L.M., A.K.S., K.S. and M.V.Y. developed expression and purification protocols. L.L.M., A.K.S. and K.S. designed constructs and prepared protein samples. M.V.Y. carried out electrophysiology experiments. E.C.T advised on cryo-EM workflow. R.A.G and E.C.T assisted with microscope operation. A.I.S. supervised the project. L.L.M., A.K.S., K.S., M.V.Y., E.C.T. and A.I.S. wrote the manuscript.

Author Information Reprints and permissions information is available at www.nature.com/reprints. The authors declare no competing financial interests. Readers are welcome to comment on the online version of the paper. Publisher's note: Springer Nature remains neutral with regard to jurisdictional claims in published maps and institutional affiliations. Correspondence and requests for materials should be addressed to A.I.S. (as4005@cumc.columbia.edu).

Reviewer Information *Nature* thanks R. Gaudet, X. Li and Y. Mori for their contribution to the peer review of this work.

METHODS

Construct. The full-length human TRPV6 (residues 1–725) and rat TRPV6 (rTRPV6, residues 1–727) were each introduced into a pEG BacMam vector[30], with the C-terminal thrombin cleavage site (LVPRG) followed by the streptavidin affinity tag (WSHPQFEK). The R470E mutation in hTRPV6 was introduced by conventional mutagenesis. The rTRPV6 construct previously used for crystallographic studies, rTRPV6* (ref. 10), was also introduced into a pEG BacMam vector but with eGFP inserted between the thrombin site and the streptavidin tag. Compared to wild-type rTRPV6, the rTRPV6* construct is C-terminally truncated by 59 residues and contains three point mutations in the ankyrin repeat domain (I62Y, L92N and M96Q).

Expression and purification. All constructs were expressed and purified similarly to $TRPV6_{cryst}$[11]. Bacmids and baculoviruses were made using a standard method[30]. The P2 baculovirus, produced in Sf9 cells (Thermo Fisher Scientific, mycoplasma negative, GIBCO #12659017), was added to HEK 293S cells lacking *N*-acetylglucosaminyltransferase I ($GnTI^-$) and grown in suspension (mycoplasma test negative, ATCC #CRL-3022) in Freestyle 293 medium (GIBCO-Life Technologies #12338-018) supplemented with 2% FBS at 37 °C and 5% CO_2. Eight to twelve hours after transduction, 10 mM sodium butyrate was added to enhance protein expression and the temperature was reduced to 30 °C. At 48–72 h post-transduction, cells were harvested by low-speed centrifugation in a Sorvall Evolution RC Centrifuge (Thermo Scientific) at 5,471*g* for 15 min, washed in phosphate-buffered saline (PBS) pH 8.0, and pelleted in an Eppendorf Centrifuge 5810 at 3,202*g* for 10 min. The cell pellet was resuspended and subjected to sonication with a Misonix sonicator (12 × 15 s, power level 8) in a buffer containing 150 mM NaCl, 20 mM Tris-HCl (pH 8.0), 1 mM βME (β-mercaptoethanol) and protease inhibitors (0.8 μM aprotinin, 2 μg/ml leupeptin, 2 μM pepstatin A and 1 mM phenylmethysulfonyl fluoride); 50 ml was used per 800 ml of HEK 293 cell culture. Subsequently, the lysate was clarified after centrifugation using a Sorvall RC-5C Plus centrifuge at 9,900*g* for 15 min, and the membranes were collected by ultracentrifugation in a Beckman Coulter ultracentrifuge equipped with a Beckman Coulter Type 45 Ti Rotor at 186,000*g* for one hour. The membranes were then mechanically homogenized, and solubilized for 1–2 h in 150 mM NaCl, 20 mM Tris-HCl pH 8.0, 1% DDM (n-dodecyl-β-D-maltopyranoside), 0.1% CHS, and 1 mM βME. Insoluble material was removed by ultracentrifugation for 40 min in a Beckman Coulter Type 45 Ti Rotor at 186,000*g* and the supernatant was added to streptavidin-linked resin and rotated for 10–14 h at 4 °C. Next, the resin was washed with 10 column volumes of wash buffer containing 150 mM NaCl, 20 mM Tris-HCl pH 8.0, 1 mM βME, 0.1% DDM, and 0.01% CHS. The bound protein was eluted in wash buffer to which 2.5 mM D-desthiobiotin was added. All constructs were purified by size exclusion chromatography using a Superose 6 column equilibrated in 150 mM NaCl, 20 mM Tris-HCl pH 8.0, 1mM βME, 0.1% DDM, and 0.01% CHS. Tris(2-carboxyethyl)phosphine (TCEP; 10 mM) was added to the peak fractions, which were pooled and concentrated for channel reconstitution in nanodiscs or amphipols. The rTRPV6 and rTRPV6* constructs were expressed and purified similarly to the hTRPV6 constructs but without the addition of CHS to any buffer. Additionally, after elution from the streptavidin-linked resin, the rTRPV6* fusion protein was concentrated to ~1.0 mg/ml and subjected to thrombin digestion at a mass ratio of 1:100 (thrombin:protein) for one hour at 22 °C with rocking, before size exclusion chromatography. Prior to reconstitution in nanodiscs or amphipols, the concentration of each construct was adjusted to approximately 1.2 mg/ml.

Reconstitution of TRPV6 protein into nanodiscs and amphipols. Both hTRPV6 and rTRPV6 were incorporated into conventional MSP2N2 lipid nanodiscs as described previously[18]. In brief, soybean polar lipid extract (Avanti #541602) was solubilized in buffer containing 20 mM Tris pH 8.0, 150 mM NaCl, 2 mM TCEP, and 15 mM DDM to create a 10-mM stock. Purified sample was mixed with the soybean polar lipid extract stock (~7.6 mg/ml) and MSP2N2 (~5.3 mg/ml) at a molar ratio of approximately 1:3:166 for both hTRPV6 (monomer:MSP2N2:lipid) and rTRPV6 (monomer:MSP2N2:lipid) and rocked at room temperature for one hour. Subsequently, 10 mg of Bio-beads SM2 (Bio-rad) pre-wet in buffer (20 mM Tris pH 8.0, 150 mM NaCl, 1mM βME) was added to 0.5 ml of mixture and the mixture was rotated at 4 °C. After one hour, an additional 10 mg of Bio-beads SM2 was added and the resulting mixture was rotated at 4 °C for ~20 h. The Bio-beads SM2 were removed by pipetting and TRPV6 reconstituted in nanodiscs was isolated from empty nanodiscs by size exclusion chromatography using a Superose 6 column equilibrated in 150 mM NaCl, 20 mM Tris-HCl pH 8.0, and 1 mM βME.

cNW11 circularized nanodiscs were prepared as described previously[31]. Purified rTRPV6* was incorporated into cNW11 (2.0 mg/ml) circularized nanodiscs using the procedure described above for the MSP2N2 nanodiscs but with a molar ratio of 1:10:267 (rTRPV6* monomer:cNW11:lipid).

For reconstitution in A8-35 amphipols (Anatrace #A835), we adapted the previously described procedure[32]. hTRPV6 or hTRPV6(R470E) was mixed with amphipols at a 1:3 mass ratio (protein:amphipols) and incubated for three hours with rotation at 4 °C. After three hours, 7–8 mg per 0.5 ml of mixture of Bio-beads SM2 pre-wet in buffer containing 20 mM Tris pH 8.0, 150 mM NaCl, 1mM βME was added to the protein–amphipols mixture to facilitate the reconstitution of TRPV6 into amphipols. The mixture was rotated for ~20 h at 4 °C and the amphipols-solubilized TRPV6 was purified as described above.

Cryo-EM sample preparation and data collection. Au/Au grids were prepared as described[33]. In brief, grids were prepared by first coating C-flat (Protochips) CF-1.2/1.3-2Au 200 mesh holey carbon grids with ~50 nm gold using an Edwards Auto 306 evaporator. Subsequently, an Ar/O_2 plasma treatment (6 min, 50 W, 35.0 s.c.c.m. Ar, 11.5 s.c.c.m. O_2) was used to remove the carbon with a Gatan Solarus (model 950) Advanced Plasma Cleaning System. The grids were again plasma treated (H_2/O_2, 20 s, 10 W, 6.4 s.c.c.m. H_2, 27.5 s.c.c.m. O_2) before sample application in order to make their surfaces hydrophilic. A Vitrobot Mark IV (FEI) was used to plunge-freeze the grids after the application of 3 μl protein solution with 100% humidity at 5 °C, a blot time of 2 or 3 s, blot force set to 3, and a wait time of 20 s. A concentration of 0.5 mg/ml was used for the nanodiscs-solubilized protein and 0.3 mg/ml for the amphipols-solubilized protein.

The hTRPV6 in nanodiscs data were collected on a Tecnai F30 Polara (C_s 2.26 mm) at 300 kV equipped with a Gatan K2 Summit direct electron detection (DED) camera (Gatan) using Leginon[34]. We collected 1,733 micrographs in super-resolution mode with a pixel size of 0.98 Å across a defocus range of −1.5 μm to −3.5 μm. The total dose, ~67 e^- $Å^{-2}$, was attained by using a dose rate of ~8.0 e^- $pixel^{-1}$ s^{-1} across 40 frames for 8 s total exposure time. We collected 1,538 hTRPV6 in amphipols micrographs and 1,301 rTRPV6* micrographs as described above. We collected 2,167 rTRPV6 micrographs as described above but in counting mode with a pixel size of 0.98 Å. The hTRPV6(R470E) data were collected on a C_s-corrected Titan Krios (FEI) equipped with a post-column GIF Quantum energy filter at 300 kV. We collected 3,540 micrographs in counting mode with a pixel size of 1.10 Å across a defocus range of −1.5 μm to −3.5 μm. The total dose, ~67 e^- $Å^{-2}$, was attained by using a dose rate of ~8.0 e^- $pixel^{-1}$ s^{-1} across 50 frames for 10 s total exposure time.

Image processing. Data were collected using the Gatan K2 Summit DED camera (Gatan) in super-resolution mode and binned 2 × 2. Frame alignment was done using MotionCor2[35]. CTF correction, using CTFFIND4[36] for the hTRPV6 in nanodiscs dataset and gCTF[37] for all other datasets, was performed on non-dose-weighted micrographs and subsequent data processing was done on dose-weighted micrographs. All other data processing, unless stated otherwise, was performed using Relion 2.0[38]. For each dataset, 1,000–2,000 particles were manually selected to generate 2D classes for use in auto-picking.

In processing the hTRPV6 in nanodiscs dataset, seven 2D classes were used for automatically picking 509,569 particles from the 1,733 collected micrographs. The particle images were binned to a pixel size of 1.96 Å per pixel and screened by 2D classification to remove aberrantly picked particles. The remaining 508,019 particles were subjected to 3D classification into 10 classes with no symmetry imposed. A density map was generated in Chimera from the crystal structure of rTRPV6 (PDB ID: 5IWK), low-pass filtered to 40 Å, and used as an initial reference. Five classes, comprising 313,369 particle images, exhibited structural features of a quality that warranted further processing. Of the five, one showed structural features of higher detail and comprised 71,582 particle images. The particle images composing this class were extracted without binning (0.98 Å per pixel), refined with C4 symmetry using the same reference (unbinned) as the prior round of classification, low-pass filtered to 40 Å, and post-processed. The resulting map was then used as a reference for the second round of 3D classification in which the particles composing the best five aforementioned classes were extracted with binning (1.98 Å per pixel) and split into ten classes with C4 symmetry imposed. Two new classes, comprising a total of 67,034 particles, exhibited structural features of a quality that warranted further processing. These 67,034 particle images were extracted without binning (0.98 Å per pixel), refined with C4 symmetry using the same reference (unbinned) as the prior round of classification low-pass filtered to 40 Å, and post-processed. The resulting map was used for the final round of 3D classification in which the two best classes from the prior round of 3D classification were without binning, and with C4 symmetry imposed, classified into 10. The four best classes, comprising 46,124 particle images, were refined together and post-processed to generate the final 3.6 Å map. This relatively small number of particles compared to the initial pool of picked up 509,569 particles indicates that the majority of picked up particles represent either artefacts or contaminants or TRPV6 molecules in alternative conformations including different gating states or unnatural conformations produced by the artificial environment of the cryo-EM grid.

Each dataset was processed using a workflow similar to that described above and the reported resolutions were estimated using the Fourier shell correlation (FSC = 0.143) criterion on masking-effect-corrected FSC curves calculated between two independent half maps[39,40]. The local resolutions were estimated with unfiltered half maps using ResMap[41] and EM density maps were visualized using UCSF Chimera[42].

The cryo-EM data collected for full-length rTRPV6 yielded a low-resolution (6.4 Å) reconstruction that was sufficient to conclude that it represents a closed-state conformation similar to rTRPV6*. As it is lacking high-resolution detail, it is not described in the main text or Extended Data.

Model building. To build the open- and closed-state models of TRPV6 in COOT[43], we used the rTRPV6* crystal structure[10] as a guide. The resulting models were refined against unfiltered half maps in real space with constraints using PHENIX[44]. The refined models were tested for overfitting (Extended Data Figs 2f, 3f, 6f, 7f) by shifting their coordinates by 0.5 Å with shake in PHENIX and building their corresponding densities in Chimera[42] from the shaken models. FSC was calculated between the densities from the shaken models, the half maps used in PHENIX refinement (work), the second half maps (free) and the unfiltered sum maps, using EMAN2[45]. The local resolutions in the transmembrane regions of our hTRPV6 in nanodiscs and hTRPV6(R470E) maps reached 2.5 Å as estimated by ResMap[41]. These high resolutions allowed us to unambiguously define the conformation of S6 in the open and closed states as well as the existence of the π-helix in the extracellular half of S6 in the open state. Structures were visualized and figures were prepared in Pymol[46].

Fura 2-AM measurements. Wild-type hTRPV6 or hTRPV6(R470E) fused to C-terminal streptavidin tag was expressed in HEK 293 cells. Cells were harvested 50–60 h after transduction by centrifugation at 600*g* for 5 min. The cells were resuspended in pre-warmed modified HEPES-buffered saline (HBS) (118 mM NaCl, 4.8 mM KCl, 1 mM $MgCl_2$, 5 mM D-glucose, 10 mM HEPES pH 7.4) containing 5 μg/ml Fura2-AM (Life Technologies) and incubated at 37 °C for 45 min. The loaded cells were then centrifuged for 5 min at 600*g*, resuspended in prewarmed, modified HBS, and incubated again at 37 °C for 25–35 min in the dark. The cells were subsequently pelleted and washed twice, then resuspended in modified HBS for experiments. The cells were kept on ice in the dark for a maximum of ~2 h before fluorescence measurements, which were conducted using a spectrofluorometer QuantaMaster 40 (Photon Technology International) at room temperature in a quartz cuvette under constant stirring. Intracellular Ca^{2+} was measured by taking the ratio of two excitation wavelengths (340 and 380 nm) at one emission wavelength (510 nm). The excitation wavelength was switched at 1-s intervals.

Electrophysiology. HEK 293 cells (ATCC #CRL-1573) were grown on glass cover slips in 35-mm dishes and were transduced with the same P2 virus as was used for large-scale protein production. Recordings were made at room temperature, 36–72 h post-transduction. Currents from whole cells, typically held at a 0 or −60 mV membrane potential, were recorded using an Axopatch 200B amplifier (Molecular Devices, LLC), filtered at 5 kHz and digitized at 10 kHz using a low-noise data acquisition system (Digidata 1440A) and pCLAMP software (Molecular Devices, LLC). The external solution contained (in mM): 140 NaCl, 6 CsCl, 1 $MgCl_2$, 10 HEPES pH 7.4 and 10 glucose. To evoke monovalent currents, 1 mM EGTA was added to the external solution. The internal solution contained (in mM): 100 CsAsp, 20 CsF, 10 EGTA, 3 $MgCl_2$, 4 NaATP and 20 HEPES pH 7.2. TRPV6 currents were recorded in response to 50-ms voltage ramps from −120 mV to 120 mV (see Extended Data Fig. 1). Data analysis was performed using the computer program Origin 9.1.0 (OriginLab Corp.).

Data availability. Cryo-EM density maps have been deposited in the Electron Microscopy Data Bank (EMDB) under accession numbers EMDB-7120 (hTRPV6 in nanodiscs), EMDB-7121 (hTRPV6 in amphipols), EMDB-7122 (hTRPV6(R470E)) and EMDB-7123 (rTRPV6*). Model coordinates have been deposited in the Protein Data Bank (PDB) under accession numbers 6BO8 (hTRPV6 in nanodiscs), 6BO9 (hTRPV6 in amphipols), 6BOA (hTRPV6(R470E)) and 6BOB (rTRPV6*). All other data are available from the corresponding author upon request.

30. Goehring, A. *et al.* Screening and large-scale expression of membrane proteins in mammalian cells for structural studies. *Nat. Protocols* **9,** 2574–2585 (2014).
31. Nasr, M. L. *et al.* Covalently circularized nanodiscs for studying membrane proteins and viral entry. *Nat. Methods* **14,** 49–52 (2017).
32. Liao, M., Cao, E., Julius, D. & Cheng, Y. Structure of the TRPV1 ion channel determined by electron cryo-microscopy. *Nature* **504,** 107–112 (2013).
33. Russo, C. J. & Passmore, L. A. Ultrastable gold substrates for electron cryomicroscopy. *Science* **346,** 1377–1380 (2014).
34. Suloway, C. *et al.* Automated molecular microscopy: the new Leginon system. *J. Struct. Biol.* **151,** 41–60 (2005).
35. Zheng, S. Q. *et al.* MotionCor2: anisotropic correction of beam-induced motion for improved cryo-electron microscopy. *Nat. Methods* **14,** 331–332 (2017).
36. Rohou, A. & Grigorieff, N. CTFFIND4: Fast and accurate defocus estimation from electron micrographs. *J. Struct. Biol.* **192,** 216–221 (2015).
37. Zhang, K. Gctf: Real-time CTF determination and correction. *J. Struct. Biol.* **193,** 1–12 (2016).
38. Kimanius, D., Forsberg, B. O., Scheres, S. H. W. & Lindahl, E. Accelerated cryo-EM structure determination with parallelisation using GPUs in RELION-2. *eLife* **5,** e18722 (2016).
39. Scheres, S. H. & Chen, S. Prevention of overfitting in cryo-EM structure determination. *Nat. Methods* **9,** 853–854 (2012).
40. Chen, S. *et al.* High-resolution noise substitution to measure overfitting and validate resolution in 3D structure determination by single particle electron cryomicroscopy. *Ultramicroscopy* **135,** 24–35 (2013).
41. Kucukelbir, A., Sigworth, F. J. & Tagare, H. D. Quantifying the local resolution of cryo-EM density maps. *Nat. Methods* **11,** 63–65 (2014).
42. Pettersen, E. F. *et al.* UCSF Chimera—a visualization system for exploratory research and analysis. *J. Comput. Chem.* **25,** 1605–1612 (2004).
43. Emsley, P., Lohkamp, B., Scott, W. G. & Cowtan, K. Features and development of Coot. *Acta Crystallogr. D* **66,** 486–501 (2010).
44. Afonine, P. V. *et al.* Towards automated crystallographic structure refinement with phenix.refine. *Acta Crystallogr. D* **68,** 352–367 (2012).
45. Tang, G. *et al.* EMAN2: an extensible image processing suite for electron microscopy. *J. Struct. Biol.* **157,** 38–46 (2007).
46. The PyMOL Molecular Graphics System (DeLano Scientific, 2002).
47. Doyle, D. A. *et al.* The structure of the potassium channel: molecular basis of K^+ conduction and selectivity. *Science* **280,** 69–77 (1998).
48. Jiang, Y. *et al.* Crystal structure and mechanism of a calcium-gated potassium channel. *Nature* **417,** 515–522 (2002).
49. Long, S. B., Campbell, E. B. & Mackinnon, R. Crystal structure of a mammalian voltage-dependent Shaker family K^+ channel. *Science* **309,** 897–903 (2005).
50. Crooks, G. E., Hon, G., Chandonia, J. M. & Brenner, S. E. WebLogo: a sequence logo generator. *Genome Res.* **14,** 1188–1190 (2004).

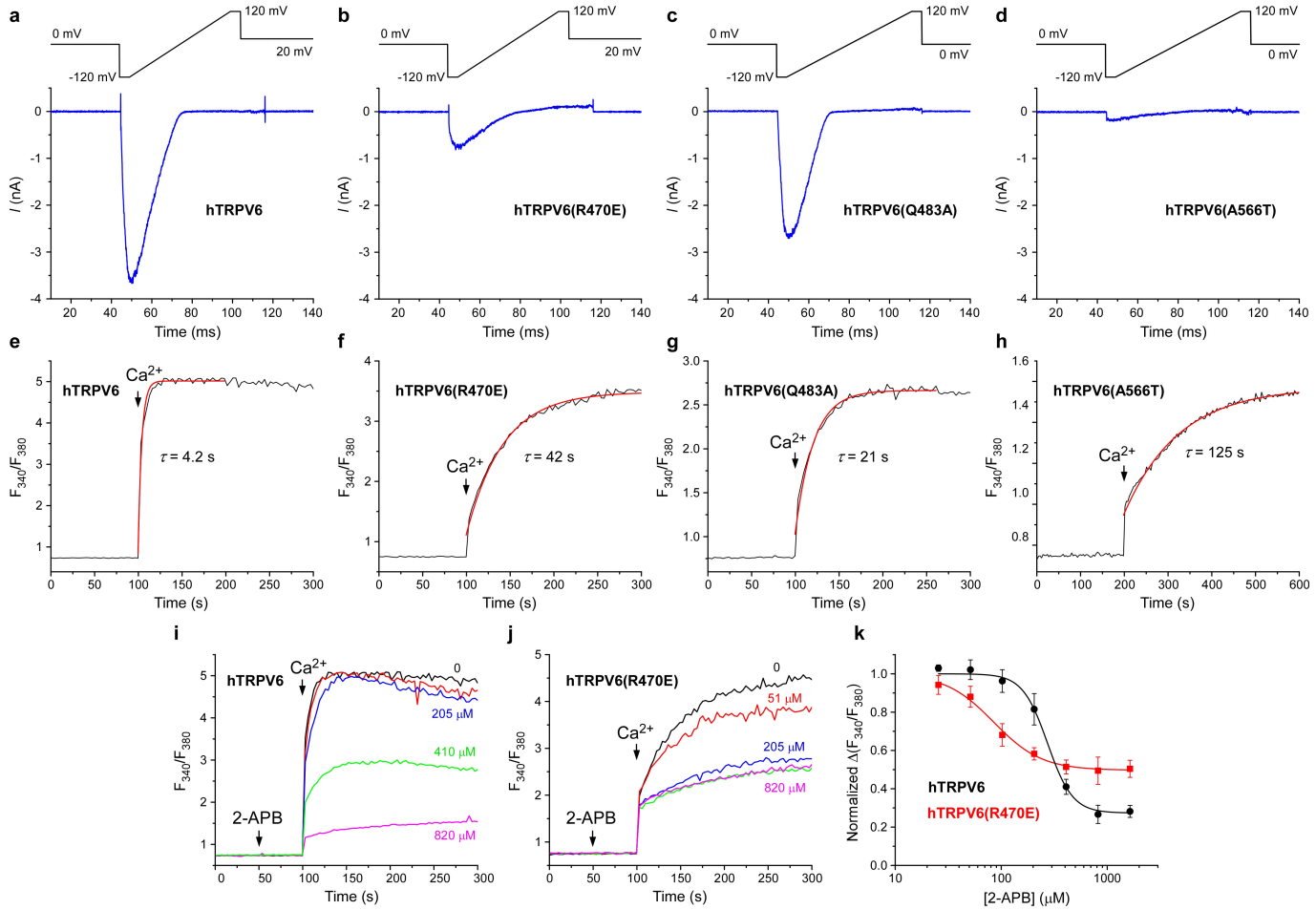

Extended Data Figure 1 | Functional characterization of wild-type and mutant hTRPV6 channels. a–d, Whole-cell patch-clamp recordings from HEK 293 cells expressing wild-type hTRPV6 (**a**), hTRPV6(R470E) (**b**), hTRPV6(Q483A) (**c**) and hTRPV6(A566T) (**d**). Leak-subtracted currents (blue) are shown in response to voltage ramp protocols illustrated above the recordings. Although the shapes of the currents for wild-type and mutant hTRPV6 channels were similar, their amplitudes were different. The average current amplitudes at −60-mV membrane potential (mean ± s.e.m.) were 3,171 ± 767 pA ($n = 11$) for wild-type hTRPV6; 918 ± 267 pA ($n = 9$) for hTRPV6(R470E); 2,239 ± 398 pA ($n = 7$) for hTRPV6(Q483A); and 145 ± 52 pA ($n = 5$) for hTRPV6(A566T). **e–h**, Kinetics of calcium uptake using Fura-2 AM ratiometric fluorescence measurements. Representative fluorescence curves are shown for wild-type hTRPV6 (**e**), hTRPV6(R470E) (**f**), hTRPV6(Q483A) (**g**) and hTRPV6(A566T) (**h**) in response to application of 2 mM Ca^{2+} (arrow). Exponential fits are shown in red, with the time constants indicated. Over five measurements, the time constants (mean ± s.e.m.) were 4.2 ± 0.5 s for hTRPV6; 47 ± 13 s for hTRPV6(R470E); 18.9 ± 0.8 s for hTRPV6(Q483A); and 121 ± 12 s for hTRPV6(A566T). At $n = 5$ and $P = 0.05$, the time constant values for wild-type and mutant channels were statistically different (two-sided *t*-test). **i, j**, Fluorescence curves for wild-type hTRPV6 (**i**) and hTRPV6(R470E) (**j**) in response to application of 2 mM Ca^{2+} after pre-incubation of cells in different concentrations of 2-APB. These experiments were repeated independently three times with similar results. **k**, Dose–response curves for 2-APB inhibition calculated for wild-type hTRPV6 (black) and hTRPV6(R470E) (red) ($n = 3$ for all measurements). The changes in the fluorescence intensity ratio at 340 and 380 nm (F_{340}/F_{380}) evoked by addition of 2 mM Ca^{2+} after pre-incubation with various concentrations of 2-APB were normalized to the maximal change in F_{340}/F_{380} after addition of 2 mM Ca^{2+} in the absence of 2-APB. Curves through the data points are fits with the logistic equation, with the mean ± s.e.m. values of half maximal inhibitory concentration (IC_{50}), 274 ± 27 µM and 85 ± 5 µM, and the maximal inhibition, 72.6 ± 2.7% and 50.3 ± 1.1%, for hTRPV6 and hTRPV6(R470E), respectively. The leftward shift of the 2-APB dose–response curve of hTRPV6(R470E), when compared to the dose–response curve of wild-type hTRPV6, indicates an increased affinity of the channel for 2-APB. This is likely to result from the R470E mutation reducing the affinity of the channel for an activating lipid ligand. On the other hand, the reduced maximum inhibition of hTRPV6(R470E) at high concentrations of 2-APB, when compared to that of wild-type hTRPV6, indicates a reduced efficacy of 2-APB that could be a result of the R470E mutation disrupting the mechanism by which 2-APB binding is allosterically coupled to channel gating.

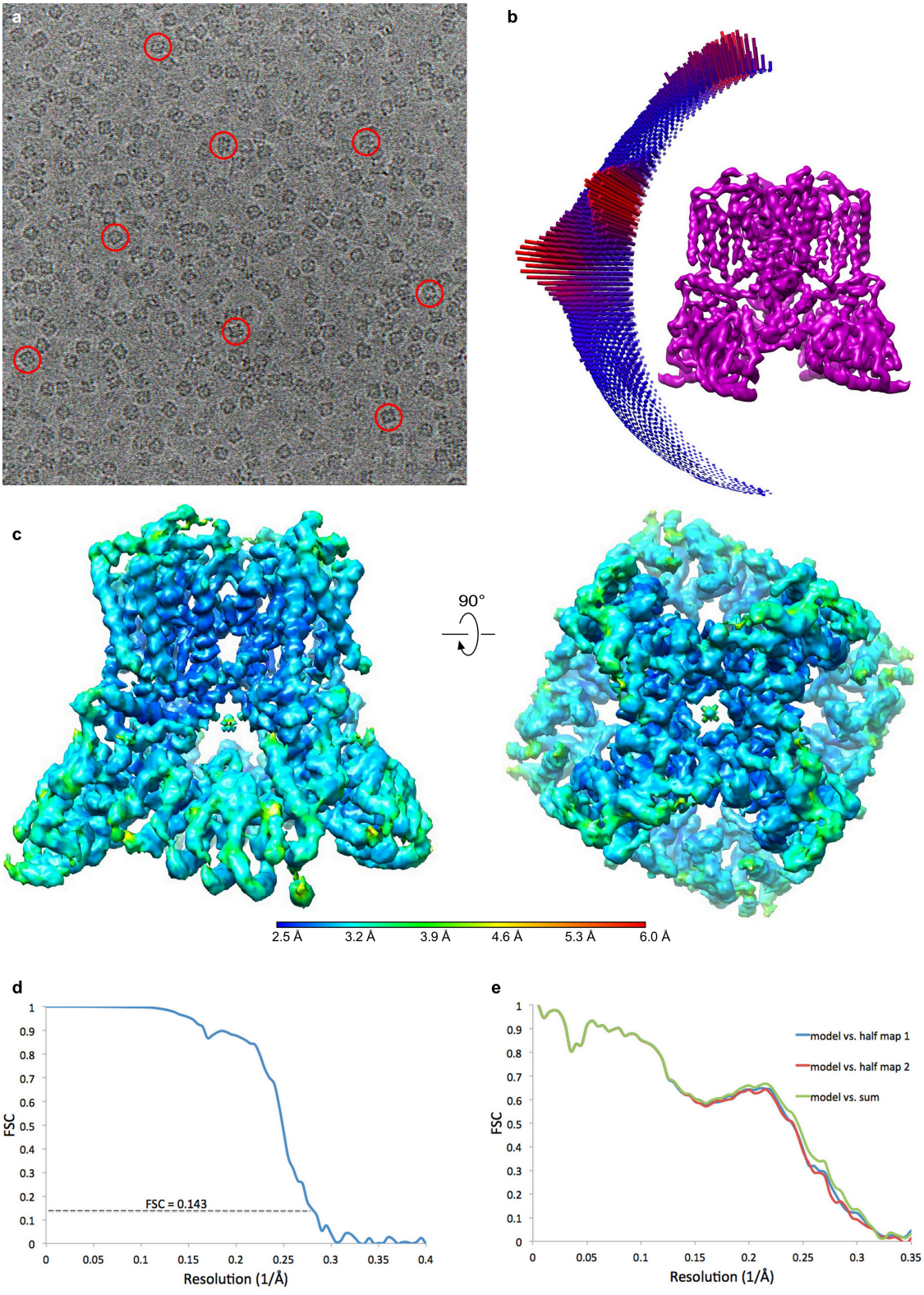

Extended Data Figure 2 | Overview of single-particle cryo-EM for hTRPV6 in nanodiscs. a, Example cryo-EM micrograph for hTRPV6 in nanodiscs with example particles circled in red. **b**, Orientations of particles that contributed to the final 3.6 Å reconstruction. Longer red rods represent orientations with more particles. **c**, Local resolution mapped on density at 0.013 threshold level (UCSF Chimera) calculated using Resmap and two unfiltered half maps, with the highest resolution observed for the channel core. **d**, FSC curve calculated between half maps. **e**, Cross-validation FSC curves for the refined model versus unfiltered half maps (only half map1 was used for PHENIX refinement) and the unfiltered summed map.

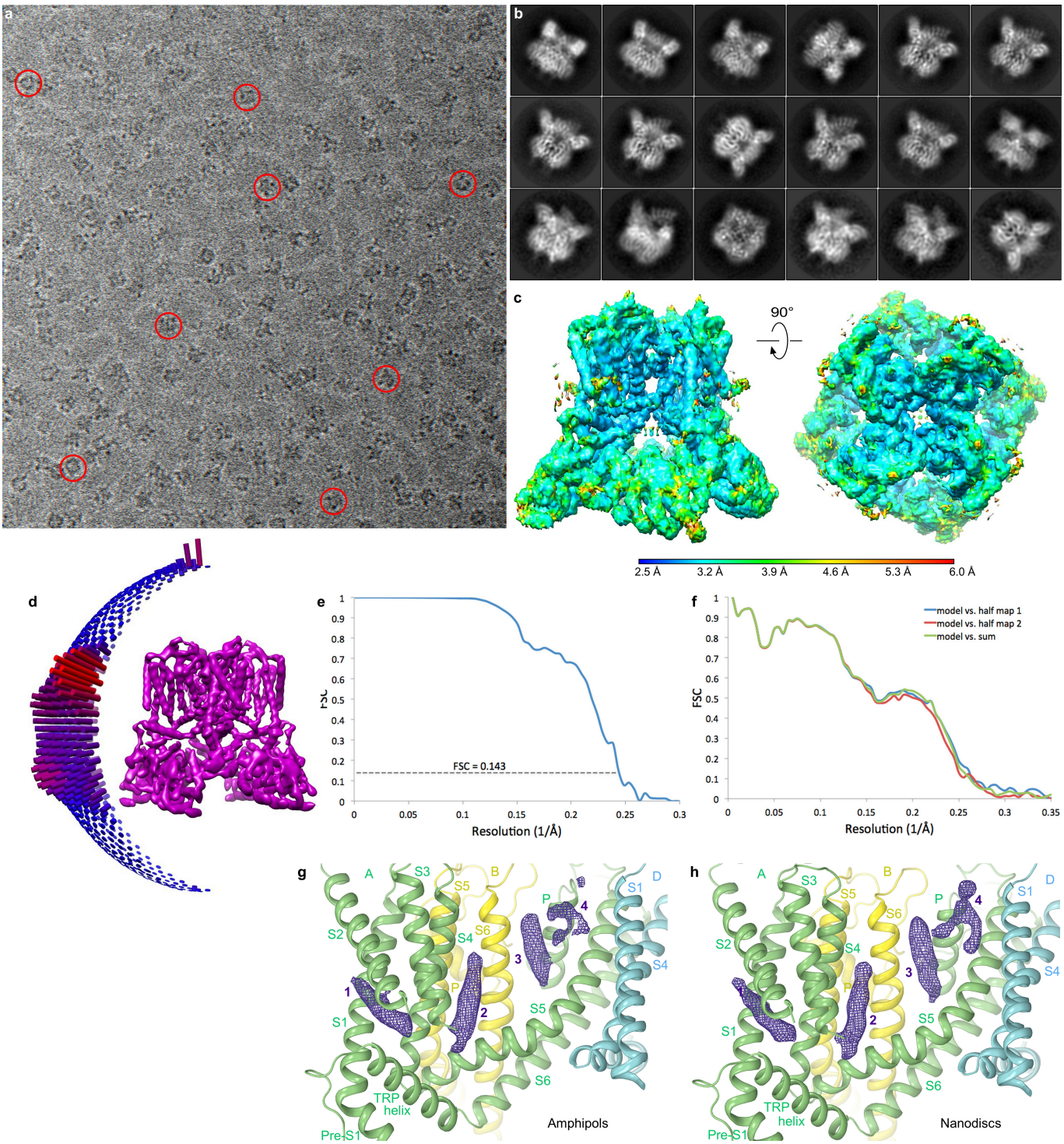

Extended Data Figure 3 | Overview of single-particle cryo-EM for hTRPV6 in amphipols and comparison to the reconstruction in nanodiscs. a, Example cryo-EM micrograph for hTRPV6 in amphipols with example particles circled in red. **b**, Reference-free 2D class averages of hTRPV6 in amphipols illustrating different particle orientations. **c**, Local resolution mapped on density at 0.01 threshold level (UCSF Chimera) calculated using Resmap and two unfiltered half maps, with the highest resolution observed for the channel core. **d**, Orientations of particles that contribute to the final 4.0 Å reconstruction. Longer red rods represent orientations that comprise more particles. **e**, FSC curve calculated between half maps. **f**, Cross-validation FSC curves for the refined model versus unfiltered half maps (only half map1 was used for PHENIX refinement) and the unfiltered summed map. **g**, **h**, Comparison of putative lipid densities for hTRPV6 in amphipols (**g**) and nanodiscs (**h**), filtered to the same (4.0 Å) resolution and shown at 3.5σ as purple mesh.

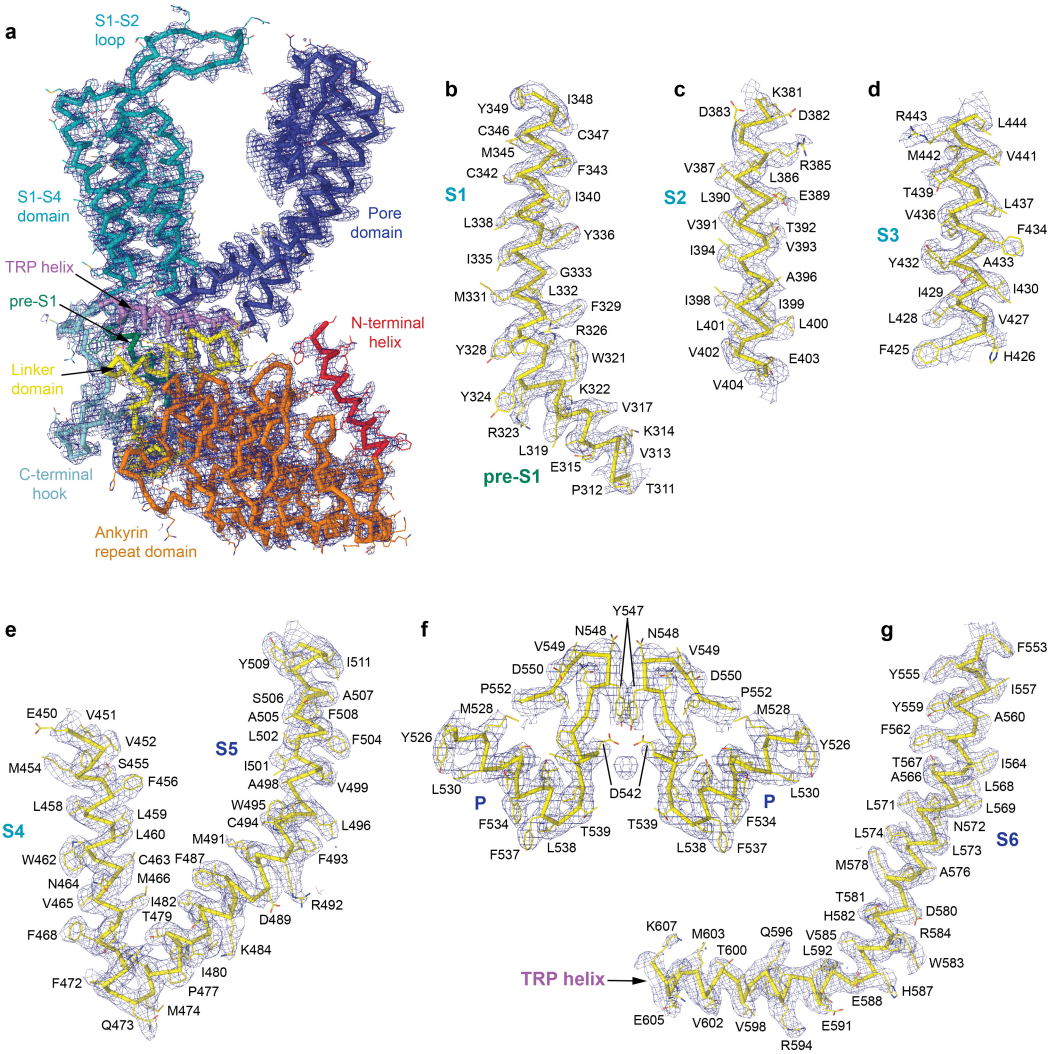

Extended Data Figure 4 | Cryo-EM density for hTRPV6 in nanodiscs. a, Cryo-EM density at 4σ for a single hTRPV6 subunit, with the protein shown in ribbon and coloured according to domains. **b**–**g**, Fragments of the hTRPV6 transmembrane domain with the corresponding cryo-EM densities.

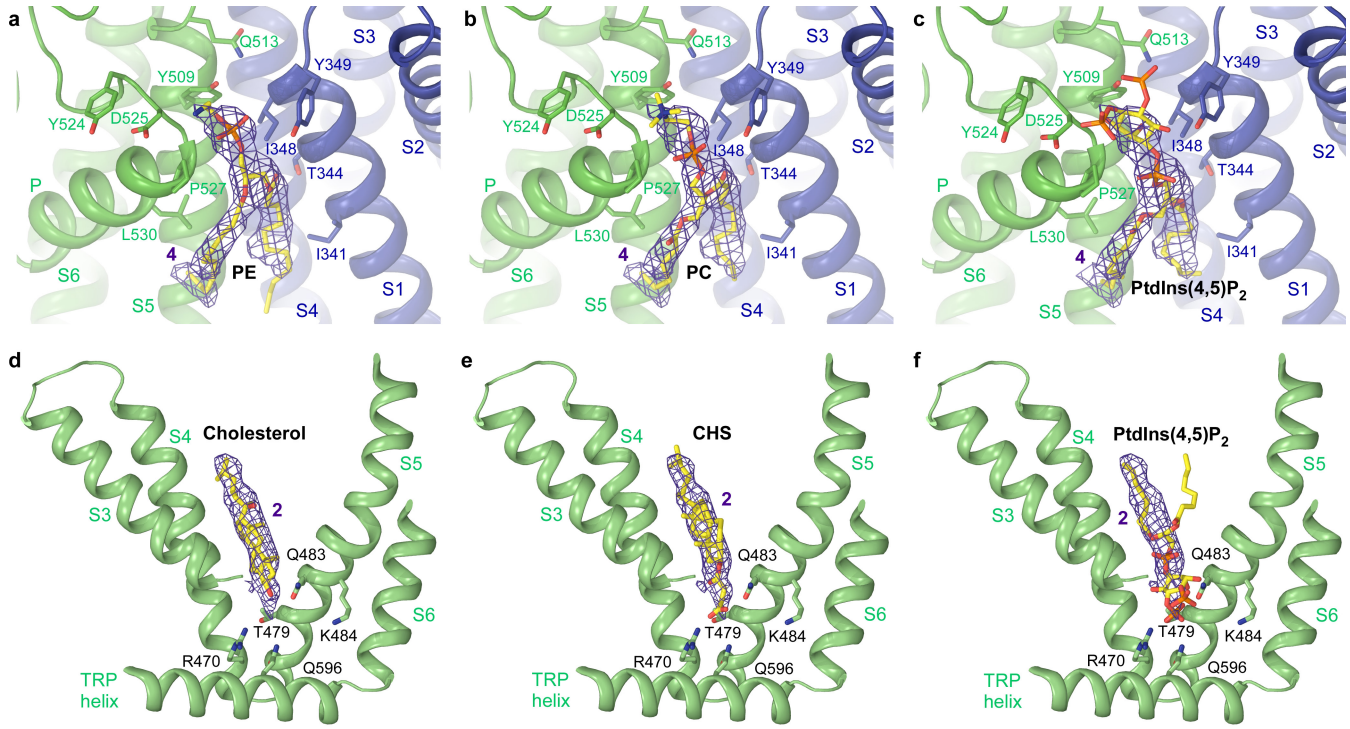

Extended Data Figure 5 | Fitting lipids into cryo-EM density. **a**–**c**, Molecules of phosphatidylethanolamine (PE, **a**), phosphatidylcholine (PC, **b**) and phosphatidylinositol 4,5-bisphosphate (PtdIns(4,5)P_2, **c**) fitted into the site 4 lipid density shown at 3.5σ as purple mesh. **d**–**f**, Molecules of cholesterol (**d**), CHS (**e**) and PtdIns(4,5)P_2 (**f**) fitted into the site 2 putative activating lipid density shown at 5.3σ.

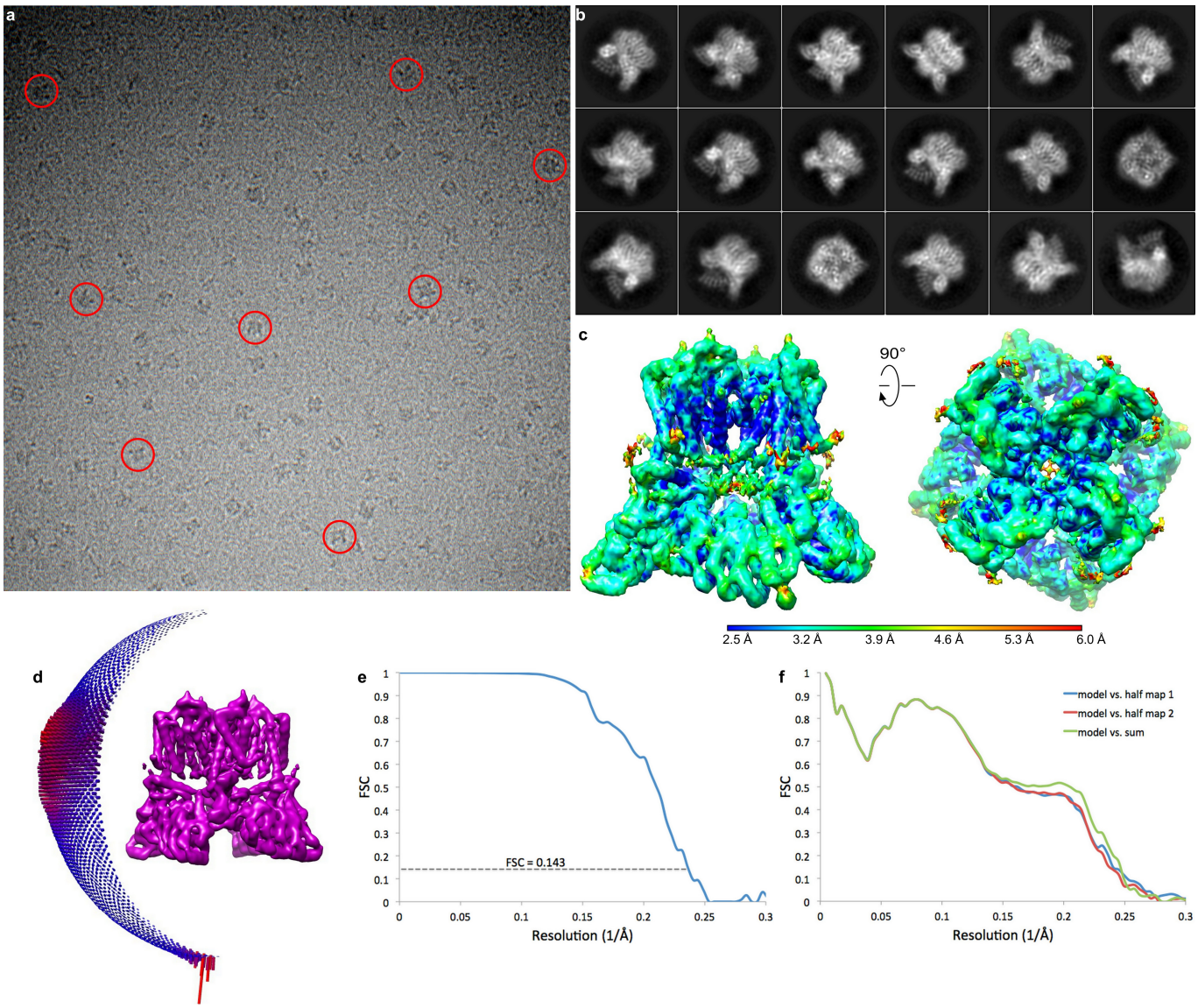

Extended Data Figure 6 | Overview of single-particle cryo-EM for hTRPV6(R470E) in amphipols. a, Example cryo-EM micrograph for hTRPV6(R470E) in amphipols with example particles circled in red. **b**, Reference-free two-dimensional class averages of hTRPV6(R470E) in amphipols illustrating different particle orientations. **c**, Local resolution mapped on density at 0.017 threshold level (UCSF Chimera) calculated using Resmap and two unfiltered half maps, with the highest resolution observed for the channel core. **d**, Orientations of particles that contribute to the final 4.2 Å reconstruction. Longer red rods represent orientations that comprise more particles. **e**, FSC curve calculated between half maps. **f**, Cross-validation FSC curves for the refined model versus unfiltered half maps (only half map1 was used for PHENIX refinement) and the unfiltered summed map.

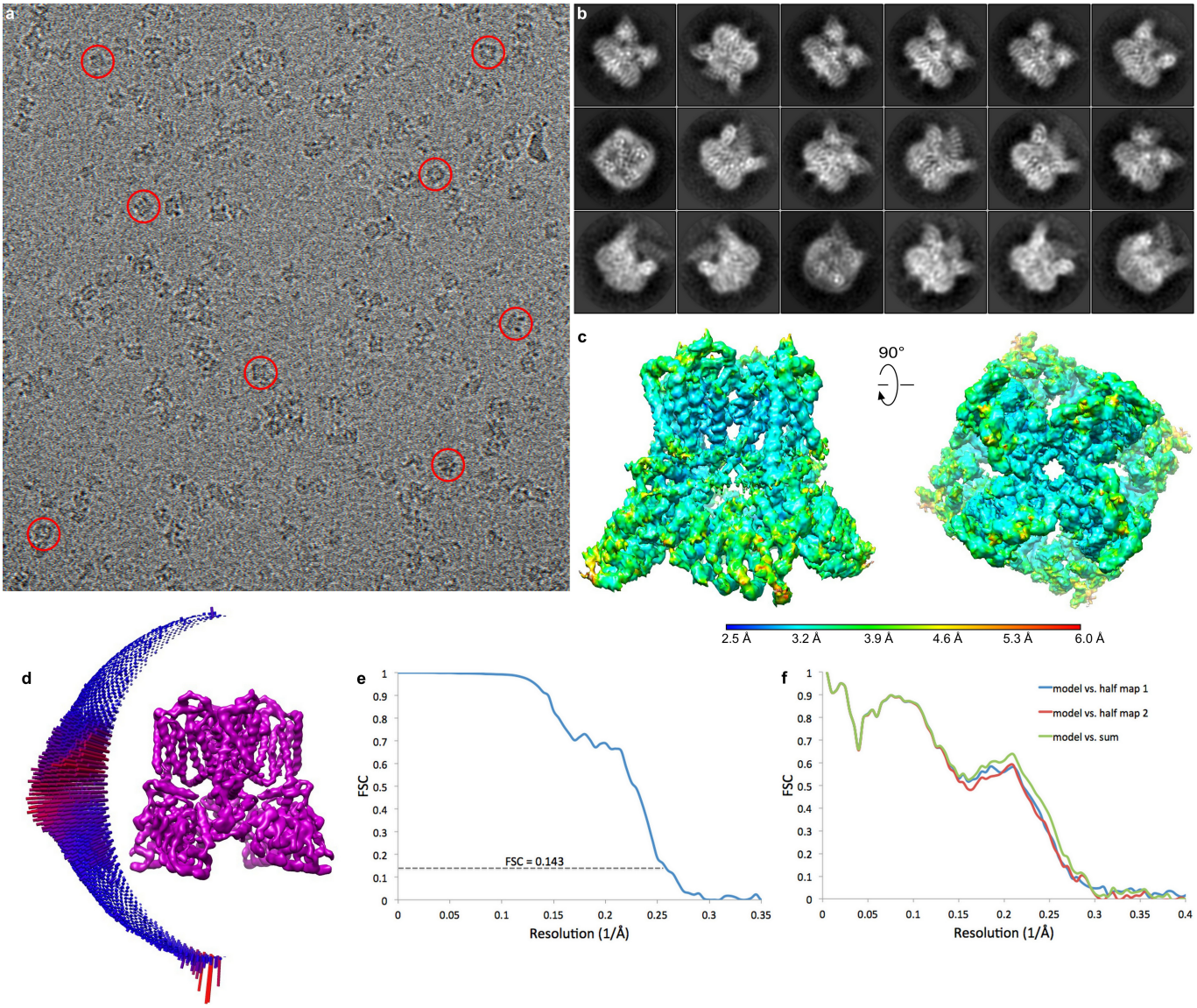

Extended Data Figure 7 | Overview of single-particle cryo-EM for rTRPV6 in CNW11 nanodiscs. a, Example cryo-EM micrograph for rTRPV6 in CNW11 nanodiscs with example particles circled in red. **b**, Reference-free 2D class averages of rTRPV6 in CNW11 nanodiscs illustrating different particle orientations. **c**, Local resolution mapped on density at 0.011 threshold level (UCSF Chimera) calculated using Resmap and two unfiltered half maps, with the highest resolution observed for the channel core. **d**, Orientations of particles that contribute to the final 3.9 Å reconstruction. Longer red rods represent orientations that comprise more particles. **e**, FSC curve calculated between half maps. **f**, Cross-validation FSC curves for the refined model versus unfiltered half maps (only half map1 was used for PHENIX refinement) and the unfiltered summed map.

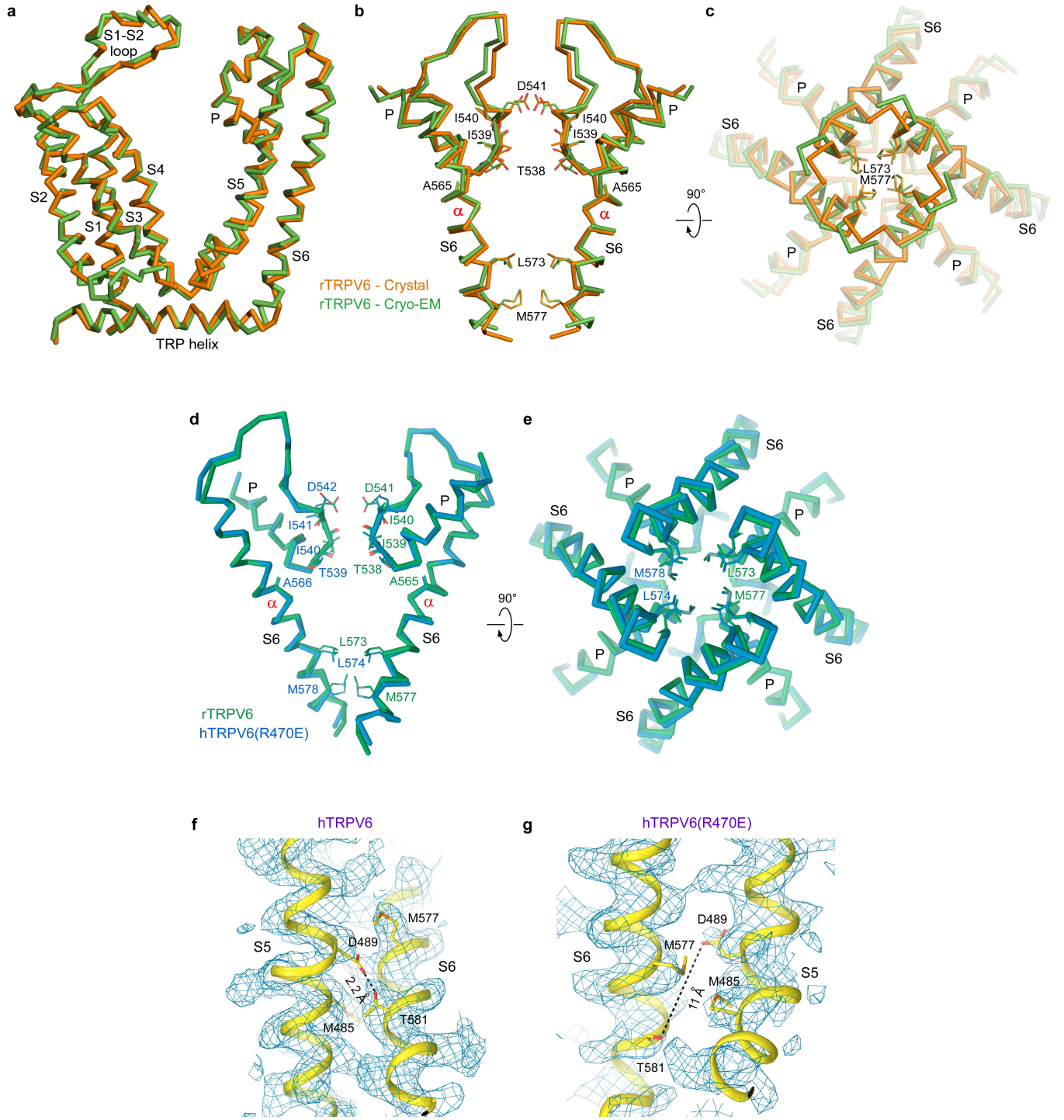

Extended Data Figure 8 | Comparison of cryo-EM and crystal structures of rTRPV6, cryo-EM structures of hTRPV6(R470E) and rTRPV6 and regions in hTRPV6 and hTRPV6(R470E) encompassing D489 and T581. a–c, Superimposed are the transmembrane domain of a single subunit (**a**), and the pore-forming region viewed parallel to the membrane (**b**) or intracellularly (**c**) from the cryo-EM (green) and crystal (orange) structures of rTRPV6. Only two of four rTRPV6 subunits are shown in **b**, with the front and back subunits omitted for clarity. Residues lining the selectivity filter and gate are shown as sticks. **d**, **e**, Superposition of the P loop and S6 in cryo-EM structures of hTRPV6(R470E) (blue) and rTRPV6 (green), viewed parallel to the membrane (**d**) and intracellularly (**e**). In **d**, only two of four subunits are shown, with the front and back subunits removed for clarity. The residues lining the pore are shown as sticks. **f**, **g**, Regions in hTRPV6 (**f**) and hTRPV6(R470E) (**g**) encompassing D489 and T581. The closest distance between D489 and T581 is indicated by dashed lines. Note, M485 and M577 either surround the potentially interacting D489 and T581 (**f**, hTRPV6) or reside between these residues (**g**, hTRPV6(R470E)), apparently preventing their interaction. Blue mesh shows cryo-EM density at 4σ.

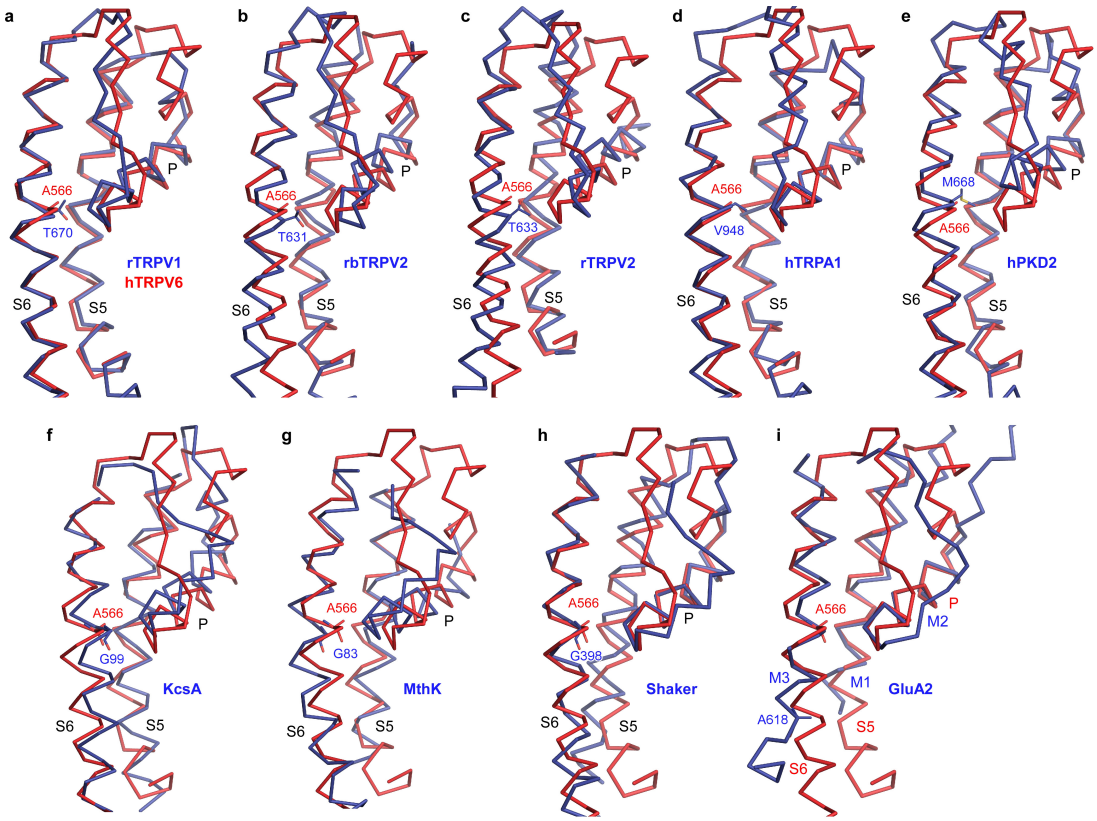

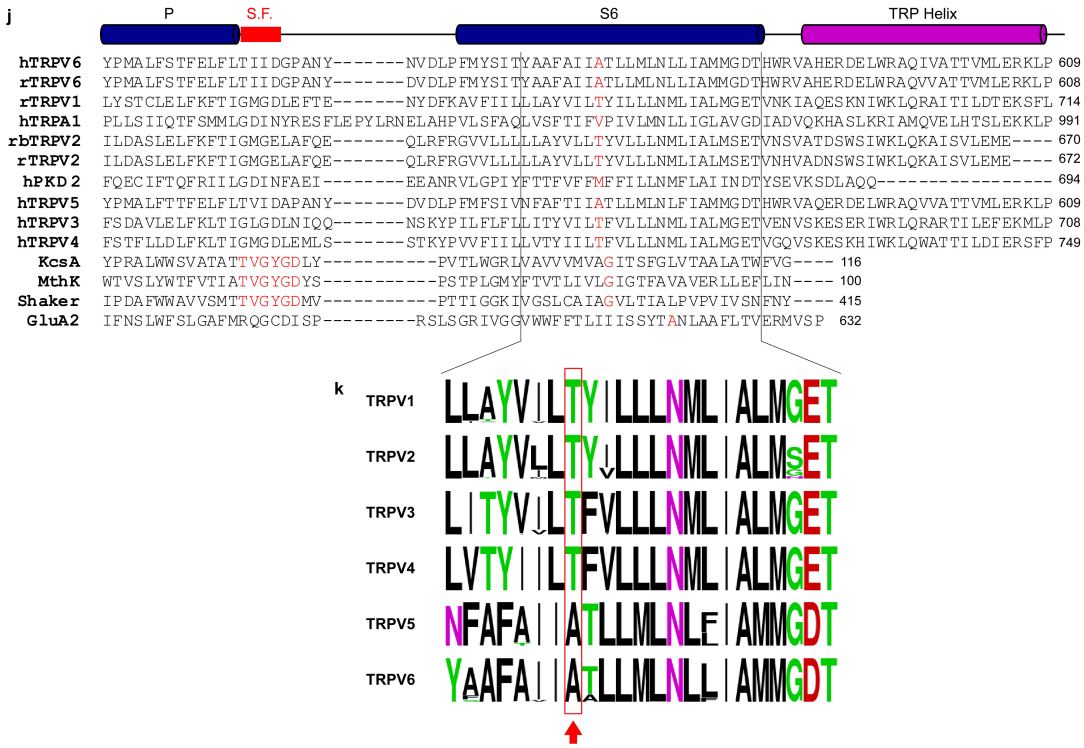

Extended Data Figure 9 | Structural superposition and sequence alignment of the pore domain in tetrameric ion channels. a–i, Pairwise superposition of the pore domain in hTRPV6 with rat TRPV1[18] (**a**, PDB ID: 5IRX; r.m.s.d. = 2.065 Å); rabbit TRPV2[21] (**b**, PDB ID: 5AN8; r.m.s.d. = 3.757 Å); rat TRPV2[24] (**c**, PDB ID: 5HI9; r.m.s.d. = 4.399 Å); human TRPA1[23] (**d**, PDB ID: 3J9P; r.m.s.d. = 1.429 Å); human PKD2[25] (**e**, PDB ID: 5T4D; r.m.s.d. = 2.676 Å); KcsA from *Streptomyces lividans*[47] (**f**, PDB ID: 1BL8; r.m.s.d. = 2.708 Å); MthK from *Methanothermobacter thermautotrophicum*[48] (**g**, PDB ID: 1LNQ; r.m.s.d. = 2.947 Å); rat Shaker[49] (**h**, PDB ID: 2A79; r.m.s.d. = 2.487 Å); and rat GluA2 AMPA-subtype iGluR[28] (**i**, PDB ID: 5WEO; r.m.s.d. = 2.044 Å). **j**, Sequence alignment for the pore region of human TRPV3–TRPV6, TRPA1 and PKD2, rat TRPV1, 2, and 6, Shaker and GluA2, rabbit TRPV2 and bacterial K^+ channels KcsA and MthK. The selectivity filter residues in K^+ channels and gating hinge residues in S6 (M3 in GluA2) are coloured red. **k**, Aligned sequence logos for TRPV channels in S6, generated by WebLogo[50] from 1,200 TRPV1–TRPV6 sequences. The red rectangle and arrow indicate the position of the alanine gating hinge in TRPV6. The relatively small side chain residues threonine or alanine next to the gating hinge alanine position in TRPV5 and TRPV6, instead of the bulky hydrophobic phenylalanine or tyrosine in TRPV1–TRPV4, might be critical for the α-to-π-helical transition in S6 during channel opening.

Extended Data Table 1 | Cryo-EM data collection, refinement and validation statistics

	hTRPV6-nanodiscs (EMDB-7120) (PDB 6BO8)	hTRPV6-amphipols (EMDB-7121) (PDB 6BO9)	hTRPV6-R470E (EMDB-7122) (PDB 6BOA)	rTRPV6* (EMDB-7123) (PDB 6BOB)
Data collection and processing				
Magnification	39,000x	39,000	105,000x	39,000x
Voltage (kV)	300	300	300	300
Electron exposure (e–/Å^2)	67	67	67	67
Defocus range (μm)	1.5 to -3.5	-1.5 to -3.5	-1.5 to -3.5	-1.5 to -3.5
Pixel size (Å)	0.98	0.98	1.10	0.98
Symmetry imposed	C4	C4	C4	C4
Initial particle images (no.)	509,569	306,784	1,243,159	248,836
Final particle images (no.)	46,124	65,259	59,298	20,808
Map resolution (Å)	3.56	4.00	4.24	3.92
FSC threshold				
Map resolution range (Å)	2.5 to 6.0	2.5 to 6.0	2.5 to 6.0	2.5 to 6.0
Refinement				
Initial model used (PDB code)	5IWK	This study	This study	This study
Model resolution (Å)	3.56	4.00	4.24	3.92
FSC threshold				
Model resolution range (Å)	2.5 to 6.0	2.5 to 6.0	2.5 to 6.0	2.5 to 6.0
Map sharpening *B* factor (Å^2)	-165	-206	-239	-173
Model composition				
Non-hydrogen atoms	19,048	19,048	19,040	19,340
Protein residues	611	611	611	611
Ligands	N/A	N/A	N/A	N/A
B factors (Å^2)				
Protein	182.9	242.8	122.0	184.2
Ligand	N/A	N/A	N/A	N/A
R.m.s. deviations				
Bond lengths (Å)	0.0079	0.0071	0.0101	0.0072
Bond angles (°)	1.33	1.3	1.46	1.37
Validation				
MolProbity score	1.97	2.06	2.22	1.98
Clashscore	7	8	5	7
Poor rotamers (%)	0.6	0.8	1.3	2.7
Ramachandran plot				
Favored (%)	88.96	87.95	88.75	88.55
Allowed (%)	11.04	12.05	11.25	11.15
Disallowed (%)	0.00	0.00	0.00	0.30